**ORIGINAL PAPER**

# Two-surface progressive failure mechanism and stability quantitative evaluation of water-induced weakening retrogressive landslides: case study for clay landslides, China

Lijuan Sun[1] · Chenjia Li[1] · Fangming Shen[1]

## Abstract

This study investigates water-induced weakening retrogressive landslides and proposes a stability evaluation method based on the two-surface progressive failure mechanism. A new test device was designed to reproduce retrogressive landslides by injecting water into the sliding zone soil from bottom to top, and the inclination angles of trailing edge fracture surfaces and horizontal displacement were measured. Then, the calculated inclination angles were taken as slice types, which were combined with the shear stress−shear displacement constitutive model and the shear displacement model of the sliding surface to characterize the stability change caused by deformation development of slopes and define the quantitative relationship between horizontal displacement and safety factor. The model test reproduces the progressive formation process of multistage sliding masses. Each sliding mass showed two failure surfaces, a bottom sliding surface and a trailing edge fracture surface. The inclination angles of the trailing edge fracture surfaces were 66~90°. Moreover, the relative errors between the theoretical and experimental inclinations were 1.33~9.09% for the model slope. For the actual landslide, the relative errors (SM3~SM7) between the theoretical and actual inclinations were 1.45~10.94%, and the relative errors of SM1 and SM2 were larger because of large deformation, so the calculation of inclination angles was not suitable for slopes with large deformation. The relative error of the total displacement was 2.33%. These tiny differences suggest that the theoretical approach is applicable. This theoretical method can infer the stability of landslide through macroscopic deformation and drilling sampling.

**Keywords** Retrogressive landslide · Water-induced weakening · Two sliding surfaces · Inclination angle · Progressive failure · Stability analysis

## Introduction

Due to the influence of natural and human factors such as rainfall, groundwater effect, engineering excavation, reservoir water level change, river erosion, water-induced weakening, and earthquakes, landslide disasters frequently occur around the world, and the types of landslides are complex and diverse (Ding et al. 2012; Liu and Li 2015; Take et al. 2015; Xu et al. 2017a, b; Azarafza et al. 2021a, b; Graber et al. 2021; Nanehkaran et al. 2021). Some of the slope bodies are affected by erosion and artificial slope cutting at the

leading edge, resulting in steep slope and instability. Cracks are caused at the trailing edge. With the development of deformation, the slope body at the rear of the trailing edge deforms and loses instability, and new sliding occurs, resulting in traction sliding failure that gradually extends to the rear of the slope from the foot of the slope, forming retrogressive landslides (Qi et al. 2018; Kennedy et al. 2021; Shan et al. 2021).

Among the various factors inducing retrogressive landslides, rainfall (Alimohammadlou et al. 2014; Zhang et al. 2016; Pan et al. 2017; Li et al. 2020), reservoir level change (Li et al. 2018; Liu et al. 2021), groundwater rise (Lv et al. 2019), irrigation (Lian et al. 2020; Graber et al. 2021), and other factors will lead to the weakening of the slope, forming a retrogressive landslide. Similar cases have been reported many times (Oezdemir and Delikanli 2009; Huang et al. 2018; Yin et al. 2020). Rainfall and reservoir-induced

✉ Lijuan Sun
sunlijuan@jlju.edu.cn

1    School of Transportation Science and Engineering, Jilin Jianzhu University, Changchun, Jilin 130118, China

**Fig. 1** A rainwater weakening-induced retrogressive landslide (Wang et al. 2021)



landslides accounted for most (Huang et al. 2020; Liu et al. 2021). Figures 1 and 2 show the retrogressive landslides induced by rainfall and reservoir water, respectively. Therefore, studying retrogressive landslides caused by water-induced weakening is of great practical significance.

Figure 3 is a schematic diagram of rain, reservoir water, groundwater, or irrigation water invading the sliding zone, which leads to weakening by water saturation. The above factors will lead to an increase in the water content of the sliding zone soil at the low position to reach saturation, resulting in an increase in pore water pressure, a decrease in effective stress, and a continuous attenuation of shear

strength, which in turn leads to local failure of slope (Jiang et al. 2014; Liao et al. 2021). With the constant expansion of the water saturation weakening range of the sliding zone soil, the whole landslide is finally unstable (Sun et al. 2021).

Water-induced weakening retrogressive landslides usually develop into multistage sliding masses and form multistage trailing edge fracture surfaces (Kennedy et al. 2021), as shown in Fig. 4. According to the field investigation, there are usually two sliding surfaces in the landslide with retrogressive sliding failure (Xu et al. 2014), which are the bottom sliding surface that controls sliding and the trailing edge fracture surface between the unstable sliding mass

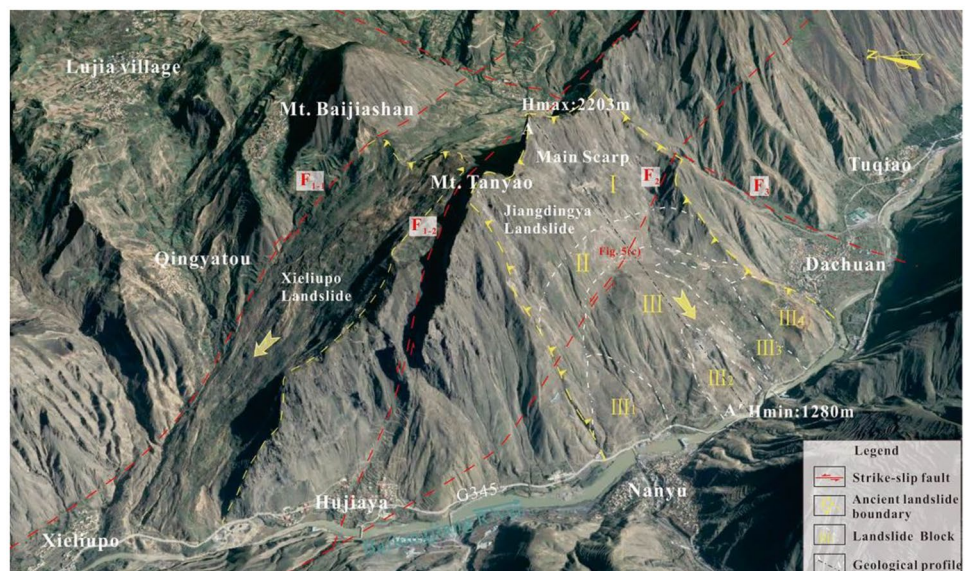**Fig. 2** A reservoir water weakening-induced retrogressive landslide (Guo et al. 2020a)
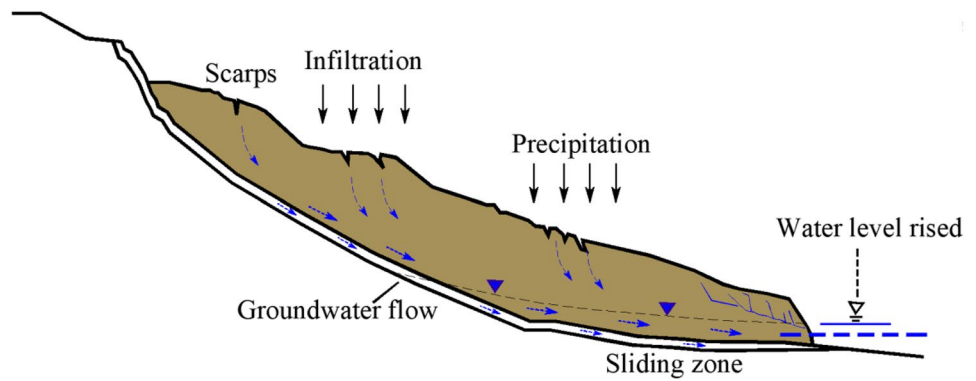
**Fig. 3** Representation of the water infiltration path and softening process of the sliding zone soil

and the rear slope. However, the failure paths of the bottom sliding surface and the trailing edge fracture surface are different. The bottom sliding surface is usually a weak interlayer or soil−rock interface parallel to the sliding direction. The trailing edge fracture surface is due to the continuous decrease in the shear strength of the bottom sliding surface caused by water infiltration, which leads to the formation of the sliding masses inside the slope and the instability of the sliding masses (Xu et al. 2014; Lian et al. 2020). This failure process is called the two-surface progressive failure mechanism in this study.

To the best of our knowledge, there is no study on the progressive failure mechanism and stability evaluation method of two sliding surfaces of retrogressive landslides considering water-induced weakening. For the field investigation of landslides, the characteristics and location of the bottom sliding zone are primarily defined by drilling. Based on the surface cracks, the boundary of the landslide and the interface between the unstable masses are judged, but the spatial form of the trailing edge cracks in the landslide is challenging to detect. In fact, the spatial distribution of the trailing edge fracture surfaces largely determines the size of the landslide and has an essential impact on the stability analysis of the landslide. Therefore, it is necessary to decide on the spatial distribution of the trailing edge fracture surfaces in the slope, and there is no suitable method to resolve it. In addition, field survey can directly obtain the deformation

information of the slope. If we can predict the stability of the slope according to the macroscopic deformation and establish a connection between the degree of deformation and the stability of the slope, it is of great significance for landslide warning (Thiebes et al. 2014).

At present, there are many studies on slope stability analysis (Amini et al. 2017; Wang et al. 2019), such as the combination of the limit equilibrium weakening coefficient and numerical methods to determine the critical slip surface and safety factor (Kainthola et al. 2013; Kumar et al. 2018), the stability analysis of discontinuous slopes by the limit equilibrium method (Thiebes et al. 2014), and the application of key block theory (Azarafza et al. 2017, 2021a, b; Azarafza and Zhu 2022). However, there are no links between the stability analysis of retrogressive landslides and slope deformation. Therefore, this paper conducts in-depth research on how to quantitatively evaluate the stability of landslides.

The indoor model test is an essential means of studying the stability of retrogressive landslides. Most previous studies used rainfall or reservoir water soaking of slopes to carry out experimental research, but these test methods were difficult to infiltrate into the sliding zone in a relatively short period of time. In most cases, erosion damage occurred on the shallow slope, and the sliding zone soil had not yet reached saturation (Regmi et al. 2014; Sun et al. 2018; Wu et al. 2015). For the water-induced weakening retrogressive landslide, the saturated sliding zone simulation is more consistent with the instability mechanism than that of the slope body.

Based on the above considerations, this paper takes the water-induced weakening retrogressive landslide as an example and develops a test device that can simultaneously stimulate the groundwater softening sliding zone and the progressive failure process of landslides. Through the saturated softening of the sliding zone in stages, the progressive failure process of two-surface instability of retrogressive landslides is understood. Based on summarizing the deformation characteristics of model tests, the progressive failure mechanical model of two sliding surfaces is established, and a landslide stability analysis method based on the progressive failure mechanism of two sliding surfaces (TSPFM) is
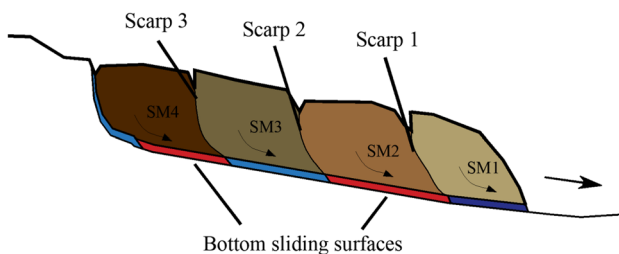


**Fig. 4** Multiple sliding masses and multiple scarps caused by water-induced weakening retrogressive landslides. SM represents the sliding mass

proposed. The method can calculate the inclination angle of the trailing edge fracture surface of the sliding mass as a new type of block division. In addition, the shear stress−shear displacement constitutive model and shear displacement model are used to link the strain-softening characteristics of sliding zone soil with the progressive failure of landslides. A specific algorithm is proposed to realize the quantitative relationship between the displacement of the sliding mass and the safety factor. Finally, this paper illustrates how to apply the TSPFM method in practical engineering and verifies the applicability of this method by practical examples.
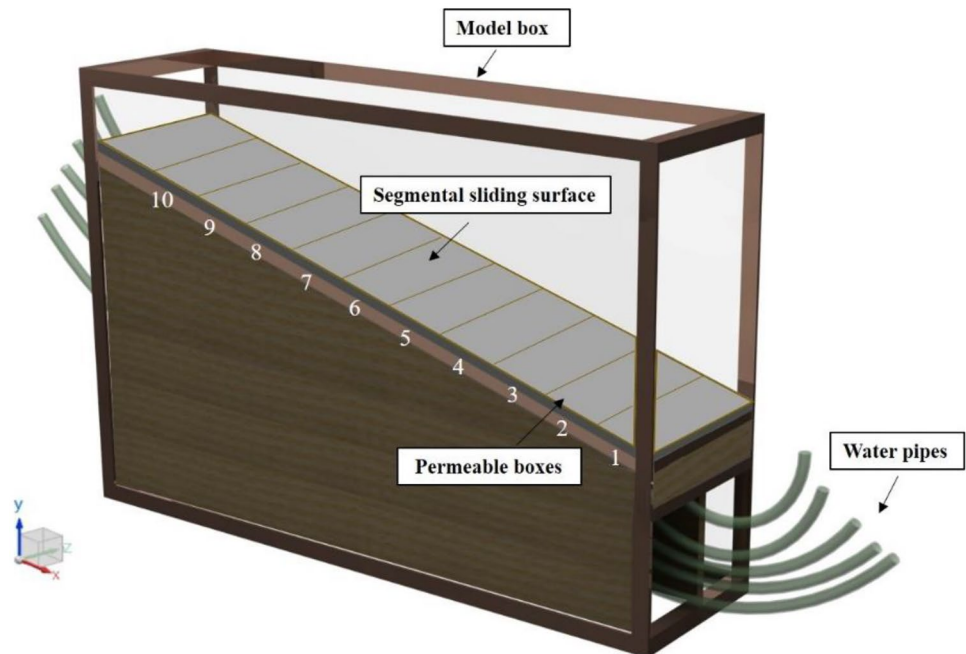
## Model tests

### Model test equipment

In this study, a model test device of the "sectional sliding surface permeation method" is designed and developed to simulate the progressive instability process of retrogressive landslides caused by the sectional saturated weakening of sliding zone soil.

The model test device comprises a model box frame, permeability system, water injection system, test system, and high-speed photography acquisition system. The size of the model box frame is 120 cm × 30 cm × 80 cm (length × width × height). The box contains the sliding body soil and sliding zone soil. The sliding bed is fixed, as shown in Fig. 5. Transparent tempered glass is used as the visual window on both sides of the model box. The

transparent coordinate calibration paper (used for accurate deformation positioning analysis) is set. Through the video tracker and digital camera installed on the side of the model box, we can observe the whole deformation process of the landslide in real time. The sliding zone permeation system is composed of 10 permeation boxes. The size of the permeation box is 30 cm × 12 cm × 2 cm, which is made of a steel plate with a wall thickness of 1 mm. A bracket with a height of 1 cm is set inside the permeation box, and the permeable stone is placed on the bracket. The water injection pipe is drawn from the bottom of the permeation box and connected to the water injection container. The water control ball valve is installed on the upper part of the water injection pipe to control the opening and closing of water and adjust the flow rate. The permeability of the permeable stone is large, and the permeability coefficient of the actual soil is as close as possible through water pressure debugging and velocity control of the water control ball valve before the test. At the beginning of the test, the sliding zone soil and sliding body soil filled the segmented sliding surface, and the water was injected into the water injection container. Each water injection pipe was adjusted to the same flow rate, and the flow through the permeable stone uniformly infiltrated into the sliding zone soil. The water content of the sliding zone soil increased and softened the soil, resulting in landslide instability. Three working conditions are designed to inject water into different permeable boxes, simulating various segmented sliding and progressive failure tests.

**Fig. 5** Model box framework

## Slope materials for model test

Clay soil landslides, as one of the six categories of landslides in China, are widely distributed. Generally, the sliding surface of cohesive soil landslides is formed due to the stress concentration at the slope toe and the softening by immersion, which follows the progressive failure principle. It is representative in the study of water-induced weakening retrogressive landslides and is more in line with the experimental principle of this paper. Therefore, this paper takes cohesive soil landslides as the research object. The survey found that the main components of clay landslides were clay and sand, so quartz sand and bentonite were selected as test materials in this study.

Sand (50 mesh quartz sand) and bentonite (600 mesh ultrafine clay) were selected as the slope materials in the model test (He et al. 2018; Zou et al. 2020), and the sliding body soil and sliding zone soil (Li et al. 2018; Liu et al. 2020) were configured by adjusting the proportion of the two materials. After many trials and adjustments, the final proportions of sliding body soil and sliding zone soil are set to 2:1 and 1:5 (the ratio of sand to soil), respectively.

To facilitate the test of the water-induced weakening mechanism of landslides, a low initial moisture content is adopted. The physical and mechanical parameters of sliding body soil and sliding zone soil are shown in Table 1, where $\gamma$ is the natural weight, $E_s$ is the compression modulus, $c$ is cohesion, and $\varphi$ is the internal friction angle. The permeability coefficient of the slope material is $(3 \sim 5) \times 10^{-6}$ m/s, which is enough to absorb all the infiltration water. According to the water content test results of sliding zone soil, the cohesion and internal friction angle decrease with increasing water content, as shown in Table 3.

## Model test condition design and test implementation

The model test is divided into three working conditions: working condition 1 (permeation boxes $2 \sim 4$), working condition 2 (permeation boxes $5 \sim 7$), and working condition 3 (permeation boxes $8 \sim 10$). The permeation box is numbered from the front shear outlet of the model box, and the order is 1, 2, and 3… 10 from front to back. The specific size of the model is shown in Fig. 6. According to multiple tests, permeation box 1 at the foot of the slope is prone to erosion
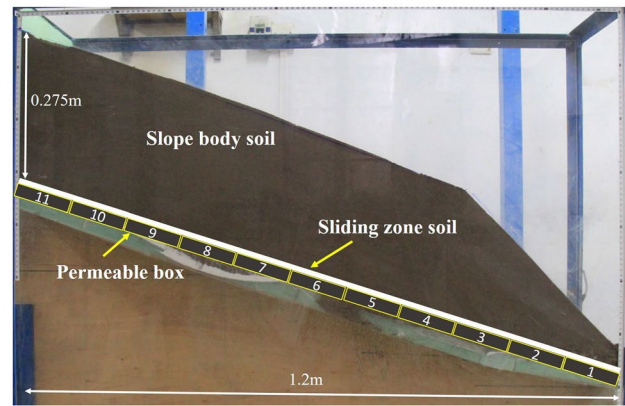
**Table 1** Physical parameters of the soils in the model slopes

| Soil type | $w$/% | $\gamma$/kN/m³ | $c$/kPa | $\varphi$/° | $E_s$/MPa |
|---|---|---|---|---|---|
| Slope body soil | 20.4 | 20.04 | 13.75 | 25.14 | 8.15 |
| Original sliding zone soil | 10.0 | 14.03 | 28.24 | 19.56 | 4.21 |
| Softened sliding zone soil | 30.0 | 17.23 | 3.68 | 9.95 | 1.19 |



**Fig. 6** The model slope consisting of a straight sliding zone and slope body

damage and affects the testing result. Therefore, it is not injected with water to avoid affecting the overall test effect.

In making the test model, the designed sliding zone is fixed at the bottom of the model box, the permeable box is laid on the pulley in turn, and the connection and the surrounding boundary are sealed. Then, using thicknesses of 2 cm and 10 cm, the amount of sliding zone soil and sliding body soil is calculated, respectively. The filling soil is layered and compacted, and the design slope is obtained. To reduce the friction between the slope and the glass on both sides, the friction reducer is added to the contact area, which significantly reduces the influence of side friction.

## Test process and result analysis

During the test, water was injected into the permeable boxes following the working conditions order. The sliding zone soil was partially saturated and weakened, and the shear strength was reduced. Then, the bottom sliding surface gradually formed, and the local slope slipped. Subsequently, the trailing edge fracture surface formed in the upper slope of the unstable sliding zone. When the bottom sliding surface and the trailing edge fracture surface are connected, the sliding mass is unstable.

Figure 6 shows the original slope model, and the test is divided into three stages. First, water is injected into working condition 1 (permeable boxes $2 \sim 4$), the first-grade sliding zone soil is weakened after absorbing water, the bottom sliding surface is gradually penetrated, the sliding body slides locally, and the trailing edge fracture surface forms inside the slope. When the bottom sliding surface and the trailing edge fracture surface are penetrated, sliding mass 1 (SM1) is completely unstable. Then, the following working conditions were started, and water was injected in working condition 2 (permeable boxes $5 \sim 7$) and working condition 3 (permeable boxes $8 \sim 10$) until the end of the working conditions. Cracks

$C_1$, $C_2$, and $C_3$ shown in Fig. 7a-d are trailing edge cracks formed with the instability of the sliding masses (SMs). Figure 8a-c show the sliding mass range formed by different sliding zone instabilities.

To accurately describe the geometric shape of the trailing edge crack inside the sliding body, the inclination angle $\theta$ of the trailing edge fracture surface is used to represent it, which is defined as the angle between the slope crack point and the horizontal plane after connecting the end of the unstable sliding zone. The inclination angles of the trailing edge fracture surface of the SMs are 76°, 83°, and 72°, respectively, as shown in Fig. 8d.

Figure 8e shows the deformation characteristics of the slope after the instability of the sliding masses. Figure 8 shows that the unstable sliding zone has a good correlation with the deformed slope, and the instability range of the sliding zone directly affects the deformation area of the landslide. The range of slope deformation caused by the instability of the first sliding zone is called SM1, and the range of slope deformation caused by the instability of the other two sliding zones is called SM2 and SM3. As the deformation of the sliding mass intensifies, the internal stress of the sliding mass is continuously adjusted, and the secondary sliding mass is gradually formed.

The test results show that the unstable bottom sliding surface correlates with the trailing edge fracture surface. Each formation of a sliding mass corresponds to the appearance of a set of bottom sliding surface and trailing edge fracture surface. That is, in the process of deformation and instability of retrogressive landslides, the sliding masses have two failure surfaces, namely, the bottom sliding surface and the trailing edge fracture surface, which are called two sliding surfaces in this paper.

## Stability analysis method for the progressive failure of two sliding surfaces

### Establishment of a mechanical model for progressive failure of two sliding surfaces

The model test shows that the instability of the retrogressive landslide is mainly manifested as the progressive failure mechanism of two sliding surfaces. For ease of calculation, the bottom sliding surface and the trailing edge fracture surface are assumed to be planes, as shown in Fig. 10. There are many cases of this assumption in actual landslides (Hu et al. 2015; Guo et al. 2020a, b), the bottom sliding surface of such landslide is usually plane, and there is an obvious interface between the upper soil layer and the base course, as shown in Fig. 9.

### New method of strip partition

#### Difference from traditional limit equilibrium slice method

At present, the slope stability analysis method adopts the limit equilibrium slice method (Huang 2013; Wu et al. 2019), and different types of division have a significant influence on the calculation accuracy. In fact, the forms of the trailing edge fracture surfaces of sliding masses are different, and they do not show a specific type. To a large extent, the spatial distribution of the trailing edge fracture surface

**Fig. 7** Generation of 3 level back scarps of the slope: **a** slope after injection 1; **b** slope after injection 2; **c** slope after injection 3; and **d** front view of the slope after injection 3
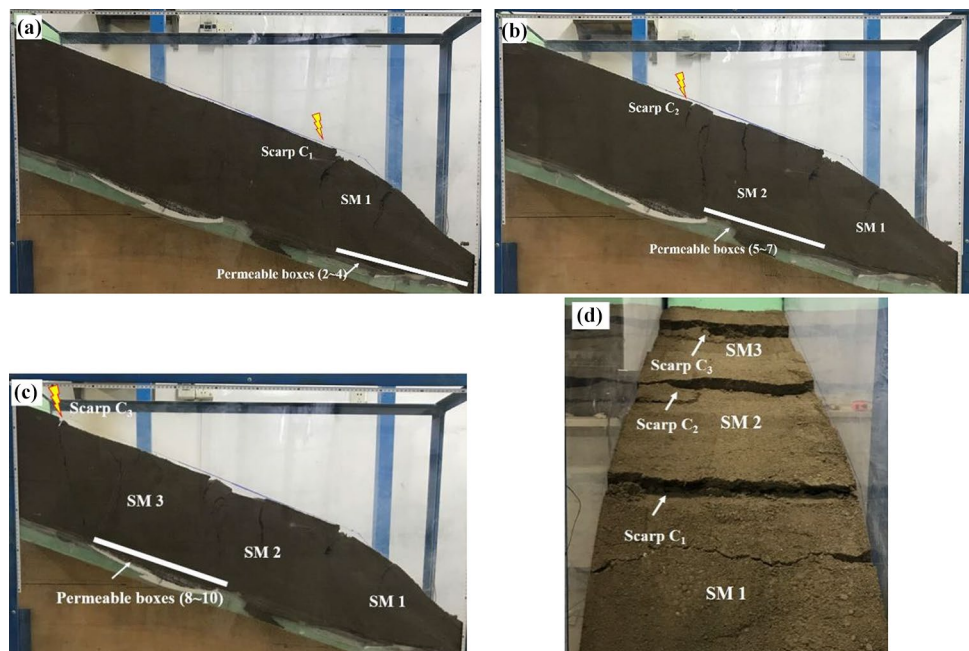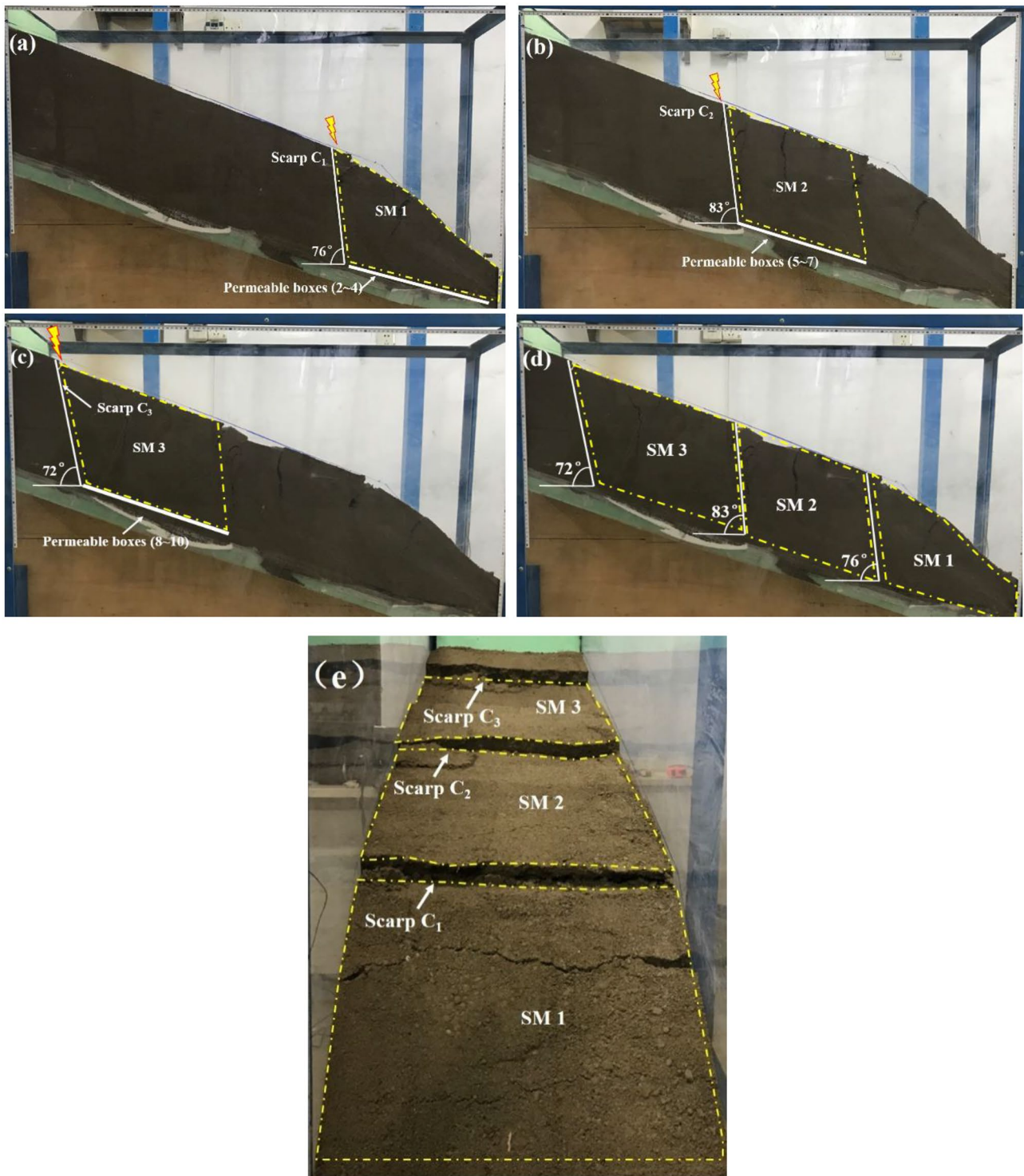
**Fig. 8** Generation of 3 sliding masses of the slope: **a** SM1 (slope after injection 1); **b** SM2 (slope after injection 2); **c** SM3 (slope after injection 3); **d** side view of the SMs; **e** front view of the SMs

determines the size of the landslide and has an important impact on the stability analysis of the landslide. Therefore, this section presents a calculation method for the trailing edge fracture surface inclination angle of retrogressive landslides, and the inclination angle is used as a block partition type for subsequent stability calculations.

For the traditional limit equilibrium analysis method (Spencer 1967; Sarma 1973), there are usually two
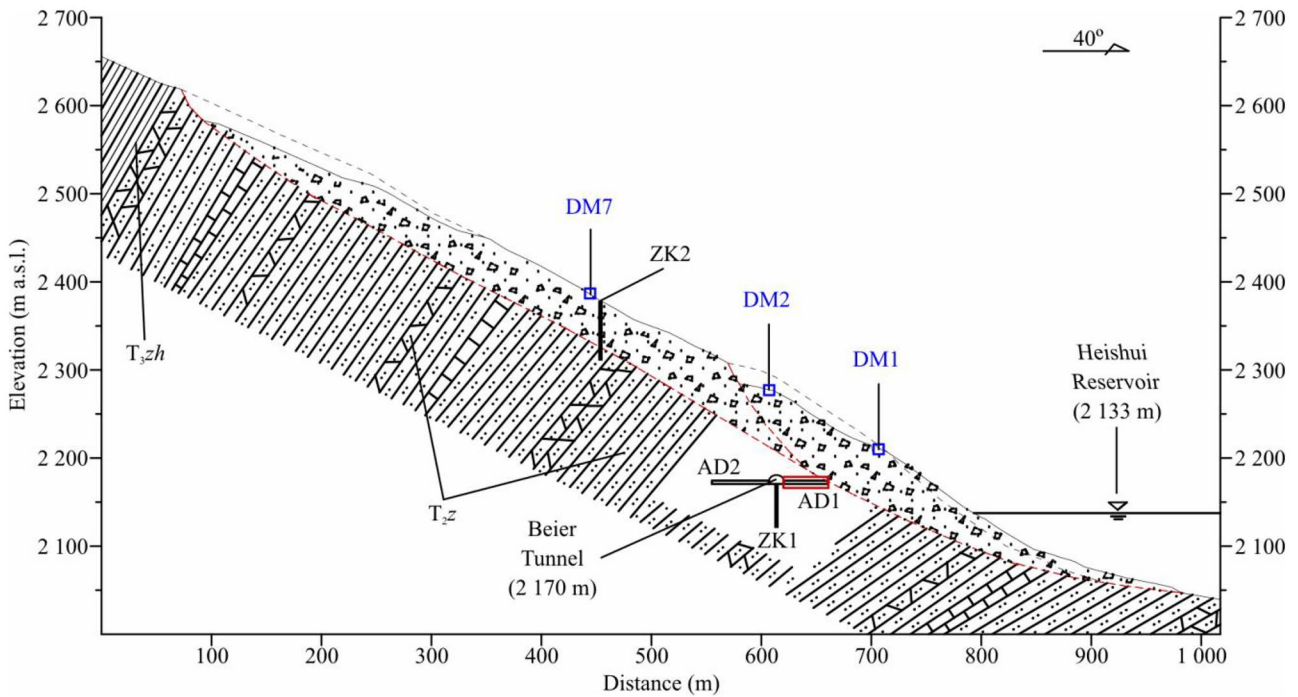
**Fig. 9** Geological profile of the Xierguazi landslide (Guo et al. 2020b)

assumptions: the first is that all parts of the failure surface have the same safety factor; the second is that when the pre-set sliding surface reaches the minimum safety factor, the whole landslide is all unstable. In fact, for the water-induced weakening retrogressive landslides, the formation of two sliding surfaces of the same sliding mass has an apparent order. The safety factors of the two sliding surfaces are not the same. First, due to the water saturation weakening of the bottom sliding surface, the shear strength decreases, and local damage occurs until the sliding surface is penetrated. As the sliding mass slips, the rear edge fracture surface gradually forms. Therefore, in the stability calculation method of this paper, the two sliding surfaces are set to have different safety factors.

## Inclination angle of trailing edge fracture surface and minimum safety factor

First, based on the Mohr−Coulomb strength criterion, the safety factor of the sliding surface is defined as the ratio of the entire anti-sliding force and the total sliding force. The shear strength of the sliding zone soil on the bottom sliding surface decreases gradually due to satura-tion weakening until the safety factor is reduced to 1. In this process, the safety factor of the trailing edge fracture surface is also gradually reduced, but it is still greater than 1. Only when the safety factor of the trailing edge fracture surface is reduced to 1 is the sliding mass com-pletely unstable.

**Fig. 10** Calculation model of retrogressive landslides
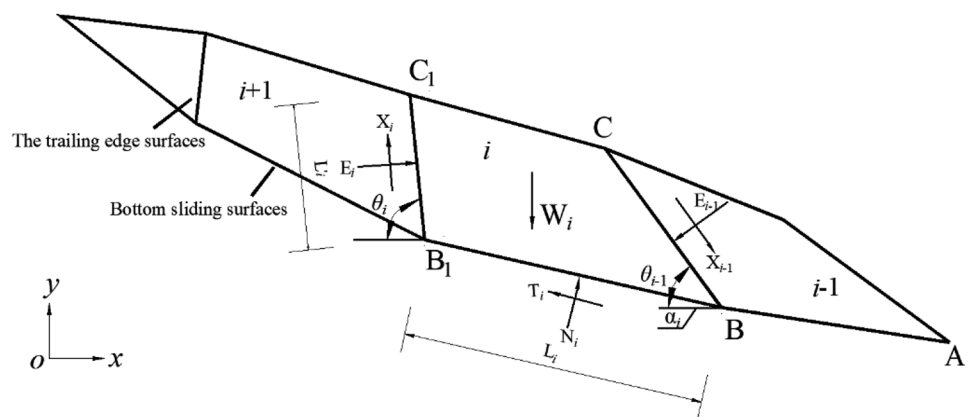
To verify the correctness of the calculation method, the test model in the "Test process and result analysis" section is selected for calculation, and the calculated soil parameters are the test parameters of the instability time of the bottom sliding zone soil in the model test. It is worth noting that when the bottom sliding zone is completely unstable, the trailing edge fracture surface still has partial shear strength, and the safety factor is greater than 1. At this time, the deformation sliding mass is in the near instability state. The inclination angle of the trailing edge fracture surface is the critical inclination angle of the final failure surface. Then, with the increase in the water content of the sliding zone soil, the sliding force increases, and the sliding mass is completely unstable. In fact, in the process of bottom sliding surface failure, there are multiple potential trailing edges, and only the trailing edge corresponding to the minimum safety factor is most likely to be damaged. Therefore, the inclination angle obtained by defining the minimum safety factor is the inclination angle of the trailing edge fracture surface. The surface where the inclination angle is located is regarded as the strip partition interface. In the "Calculation of the new segmentation method" section, the inclination angle of the trailing edge fracture surface corresponding to the minimum safety factor is examined by establishing the objective function.

## Calculation of the new segmentation method

Figure 10 shows the landslide calculation model, where $W_i$ is the weight of sliding mass $i$; $N_i$ is the positive pressure acting on the sliding surface of sliding mass $i$; $T_i$ is the shear force acting on the sliding surface of sliding mass $i$; $E_{i-1}$ and $E_i$ are the positive pressures acting on the left and right sides of sliding mass $i$, respectively; $X_{i-1}$ and $X_i$ are the shear forces acting on the left and right sides of sliding mass $i$, respectively; $l_i$ is the sliding surface length of sliding mass $i$; $l_i$' is the length of the trailing edge fracture surface of sliding mass $i$; $\alpha_i$ is the inclination angle of the bottom sliding surface of sliding mass $i$; and $\theta_{i-1}$ and $\theta_i$ are the inclination angles of the trailing edge fracture surfaces of sliding masses $i-1$ and $i$, respectively. In this calculation model, according to the limit equilibrium condition of sliding masses and Mohr−Coulomb strength failure criterion, the equilibrium equation of any sliding mass $i$ is established.

Assuming that the sliding mass $i$ has a safety factor $F_i$, the bottom sliding surface $BB_1$ satisfies the limit equilibrium condition:

$$T_i = \frac{c_{zi} \cdot l_i + N_i \cdot \tan\left(\varphi_{zi}\right)}{F_i} \tag{1}$$

After the sliding of the bottom sliding surface $BB_1$, the trailing edge fracture surface $B_1C_1$ is formed, and $B_1C_1$ is a tensile-shear failure surface (the crack depth caused by tensile failure is small, which is ignored). Then, there are:

$$X_i = c_{mi} \cdot l'_i + E_i \cdot \tan\left(\varphi_{mi}\right) \tag{2}$$

Under the limit state, sliding mass $BB_1C_1$ satisfies static equilibrium, and the equilibrium equation in the horizontal direction is:

$$T_i \cdot \cos\left(\alpha_i\right) - N_i \cdot \sin\left(\alpha_i\right) + X_i \cdot \cos\left(\theta_i\right) - E_i \cdot \sin\left(\theta_i\right) = 0 \tag{3}$$

The equilibrium equation in the vertical direction is:

$$T_i \cdot \sin\left(\alpha_i\right) + N_i \cdot \cos\left(\alpha_i\right) + X_i \cdot \sin\left(\theta_i\right) + E_i \cdot \cos\left(\theta_i\right) - W = 0 \tag{4}$$

In the above formula, $c_{zi}$ is the cohesion of the bottom sliding surface of sliding mass $i$, $\varphi_{zi}$ is the internal friction angle of the bottom sliding surface of sliding mass $i$, and $c_{mi}$ and $\varphi_{mi}$ are the cohesion and the internal friction angle of the trailing edge fracture surface of sliding mass $i$, respectively.

Since the sliding mass $BB_1C_1$ is in the limit equilibrium, it meets the torque balance simultaneously. For the $B_1$ point, there are:

$$N_i \cdot l_{Ni} - E_i \cdot l_{Ei} + W_i \cdot l_{Gi} = 0 \tag{5}$$

where $l_{Ei}$, $l_{Ni}$, and $l_{Gi}$ are the force arms of $E_i$, $N_i$, and $W_i$, respectively, as determined by the geometry in Fig. 10. The safety factor $F_i$ can be obtained by combining the above formulas. When the safety factor $F_i$ is the smallest, the corresponding trailing edge fracture angle $\theta_i$ is obtained.

To simplify the calculation results:

$$a = \cos\alpha, b = \cos\theta, c = \sin\alpha, d = \sin\theta, e = \tan\varphi_z, f$$
$$= \tan\varphi_m, m = l_{AB}, n = l_{BC}$$

The expression of the safety factor of sliding mass $i$ is:

$$F_i = \frac{-\left\{1 \cdot \left(\begin{array}{c} 2abcefmW + 2abdefnW + 2dc^2efmW + 2d^2cefnW + 3m^3bcfc_z - 3m^3adfmc_z + 2bc^2emW + 2bcdenW - 3bcec_mn^2 \\ -2acdemW - 2aed^2nW + 3adec_mn^2 - 3m^3abc_zm - 3cdc_zm^3 - 2cefnW - 2defmW - 2bemnW - aenW - 3c_zmn \end{array}\right)\right\}}{\left(\begin{array}{c} 2ad^2fnW - 2bdcfnW + 2adcfmW - 2bc^2fmW + 2d^2cnW + 2abdnW + 2dc^2m - 3dcc_mn^2 + 2abcmW \\ -3abc_mn^2 - 3mbfW + 2bfmW - 2afnW + 3mdW - 2dmW - 2dmW - 3mc_mn + cnW \end{array}\right)} \tag{6}$$

**Fig. 11** Sliding shear displacement vector diagram
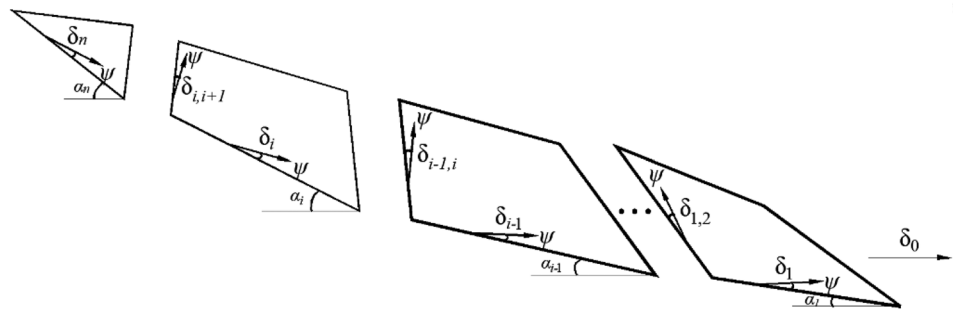


Note that Formula (6) is derived on the assumption that the inclination angle $\theta$ of trailing edge fracture surface is known. For a specific landslide, the derivative of Eq. (8) to $\theta$ can be obtained. When the derivative is 0, $F_i$ is obtained, but the derivative calculation is too complex. Considering the actual failure characteristics of the retrogressive landslide, this paper assumes that each $\theta$ value is in the maximum search range and calculates the safety factors corresponding to different $\theta$ values, where the inclination angle corresponding to the minimum safety factor is calculated.

## Study on the shear stress−shear displacement constitutive model of the sliding surface

The stress−strain model of the sliding zone directly reflects the development process and evolution characteristics of landslides. The joint constitutive model proposed by Lu overcomes the defects of the traditional ideal elastoplastic model (Lu et al. 2015; Lu 2015) and can describe the whole process characteristics of strain-softening materials under different normal stresses. Wang et al. (2018) extended the above model to fit the relationship between shear stress and shear displacement, as shown in Eq. (7):

$$\tau = G\delta\left[1 + \delta^m/s\right]^\xi \tag{7}$$

In the formula, $\tau$ and $\delta$ are the shear stress and shear displacement, respectively. $G$ is the initial slope of the shear stress–shear displacement curve of sliding zone soil; $m$, $s$, and $\xi$ are constant coefficients varying with normal stress; the unit of $\tau$ is Pa, kPa, or MPa; the unit of $\delta$ is m or mm; and $m$, $s$, and $\xi$ are nondimensional parameters.

This model has the following properties:

1. The peak shear displacement $\delta_{peak}$ is:

$$\delta_{peak} = \sqrt[m]{-s/(1 + m\xi)} \tag{8}$$

The corresponding peak stress $\tau_{peak}$ is:

$$\tau_{peak} = G\sqrt[m]{-s/(1 + m\xi)}\left[1 - 1/(1 + m\xi)\right]^\xi \tag{9}$$

2. Under a specific normal stress state, the peak stress of the model is equal to the critical state shear stress calculated by the Mohr−Coulomb failure criterion. That is, the peak stress can also be expressed as:

$$\tau_{peak} = c + \sigma_n \tan\varphi \tag{10}$$

3. $s$ is a parameter related to the normal stress of the sliding surface, which can be calculated by the following formula:

$$s = -\frac{\left(c_n + \sigma_n \tan\varphi\right)^2}{G^2}\left(\frac{2\xi}{1 + 2\xi}\right)^{-2\xi}(1 + 2\xi) \tag{11}$$

4. $\xi$ is the parameter describing the softening characteristics of soil, which is related to the features of the material itself. When $\xi = -0.5$, it can be used to describe the ideal elastoplastic material; when $\xi = 0$, it represents the ideal elastic material; when $-0.5 < \xi < 0$, the characteristics of strain hardening materials are described; and when $-1 < \xi \le -0.5$, it is used to characterize the attributes of strain-softening materials.

## Shear displacement model distributed along the sliding surface

To consider the influence of displacement factors, the displacement coordination equation of the bottom sliding surface is introduced to characterize the shear displacement relationship between adjacent sliding masses. Consider the following assumptions: (1) assuming that only small deformation occurs on the slope; (2) the compression deformation inside the strip block and the separation and overlap in the slip process are not considered; (3) shear slip is considered in the sliding surface shear displacement of all sliding masses; and (4) considering the dilatancy characteristics, the shear displacement relationship between the sliding mass $i$ and sliding mass $i-1$ are shown in Figs. 10 and 11:

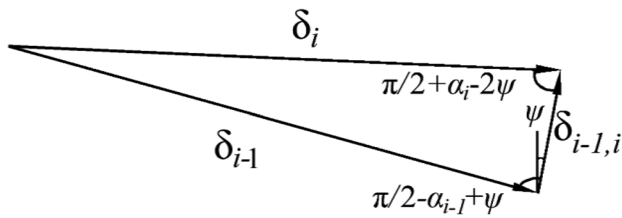According to the displacement relationship shown in Fig. 12 and the trigonometric function, we can obtain:

**Fig. 12** Displacement coordination between adjacent slices

$$\delta_i = \delta_{i-1} cos(\alpha_{i-1} - 2\psi)/cos(2\psi - a_i) \qquad (12)$$

where $\delta_i$ and $\delta_{i-1}$ are the slip surface shear displacements of sliding masses $i$ and $i-1$, $\psi$ is the dilatancy angle, and $\alpha_i$ and $\alpha_{i-1}$ are the bottom inclination angles of sliding masses $i$ and $i-1$.

Accordingly, the shear displacement formulas of other sliding masses represented by the horizontal displacement of sliding mass $i$ can be obtained, as shown in Formulas (13) and (14):

$$\delta_i = \delta_0 p(\alpha_i) \qquad (13)$$

$$p(\alpha_i) = \frac{1}{\cos(\alpha_1 - \psi)} \frac{\cos(\alpha_1 - 2\psi)}{\cos(2\psi - \alpha_i)} \qquad (14)$$

In the formula, $\delta_0$ is the horizontal displacement of sliding mass 1, and $p(\alpha_i)$ is the displacement coordination coefficient between adjacent sliding masses.

## Stability analysis of two-surface progressive failure (TSPFM)

This section is based on improving the previous limit equilibrium analysis method. (1) A new strip partition type is adopted, and the bottom sliding surface and the trailing edge fracture surface of the sliding mass have different safety factors. (2) Combined with the sliding surface $\tau$-$\delta$ constitutive model and shear displacement model, the strain-softening characteristics of sliding zone soil are connected with the progressive failure process of retrogressive landslides, and a specific algorithm is proposed to characterize the quantitative relationship between the horizontal displacement and safety factor.

Taking the sliding mass $i$ as an example, as shown in Fig. 13, $\delta_0$ and $\delta_i$ are the horizontal displacements of sliding mass $i$. The specific calculation process is as follows:

$$T_i \cdot cos(\alpha_i) - N_i \cdot \sin(\alpha_i) + X_i \cdot \cos(\theta_i) - E_i \cdot \sin\theta_i = 0 \qquad (15)$$

$$T_i \cdot \sin\alpha_i + N_i \cdot \cos\alpha_i + X_i \cdot \sin(\theta_i) + E_i \cdot \cos\theta_i - W_i = 0 \qquad (16)$$

$$N_i \cdot l_{Ni} - E_i \cdot l_{Ei} + W_i \cdot l_{Gi} = 0 \qquad (17)$$
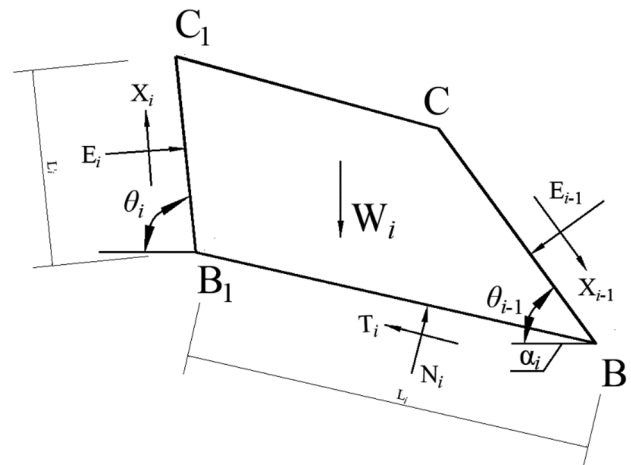


**Fig. 13** Mechanical analysis of sliding mass $i$

$$X_i = C_{mi} \cdot l_i' + E_i \cdot \tan(\varphi_{mi}) \qquad (18)$$

The frictional stress of the sliding surface is:

$$\tau_i = G_i\, \delta_i [1 + \delta_i^{m_i}/s_i]^\xi \qquad (19)$$

The anti-skid resistance is:

$$T_i = G_i\, \delta_i [1 + \delta_i^{m_i}/s_i]^\xi l_i \qquad (20)$$

Mohr–Coulomb criterion:

$$T_{if} = c_i l_i + N_i \tan \varphi_i \qquad (21)$$

The normal stress of the sliding surface is:

$$\sigma_i = N_i/l_i \qquad (22)$$

$s_i$ is a parameter related to the positive stress of the sliding surface, and it can be obtained from Eq. (23):

$$s_i = -\frac{(c_i + \sigma_i \tan \varphi_i)^2}{G_i^2}\left(\frac{2\xi}{1+2\xi}\right)^{-2\xi}(1+2\xi) \qquad (23)$$

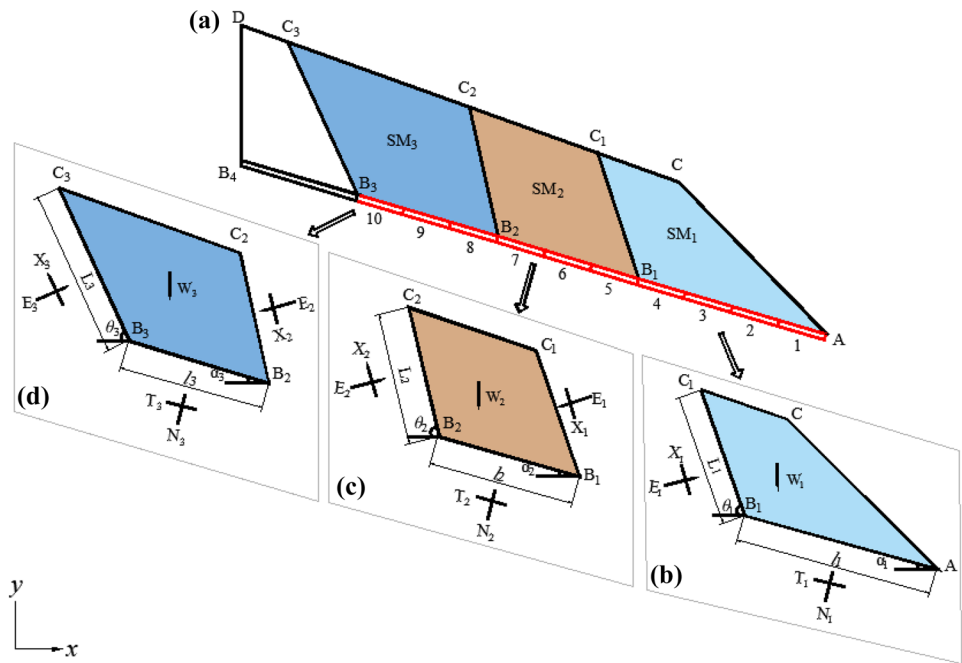The safety factor of the sliding mass $i$ is defined as:

$$K_i = T_{if}/T_i \qquad (24)$$

Substituting Eqs. (7) and (13) into Eq. (20), $T_i$ can be expressed as:

$$T_i = G\delta_0 p(\alpha_i)[1 + \delta_0^m p^m(\alpha_i)/s_i]^\xi \qquad (25)$$

$$K_i = \frac{T_{if}}{T_i} = \frac{c_i l_i + N_i \tan \varphi}{G\delta_0 p(\alpha_i)[1 + \delta_0^m p^m(\alpha_i)/s_i]^\xi} \qquad (26)$$

**Fig. 14** Schematic of slope: **a** original slope; **b** force analysis of sliding mass 1; **c** force analysis of sliding mass 2; **d** force analysis of sliding mass 3; SM represents sliding mass



The calculation steps are as follows:

Sliding mass $i$ ( $i = 1, 2, 3 \ldots n$):

1. The cohesion ($c_{wi}$), internal friction angle ($\varphi_{wi}$), and shear modulus ($G_{wi}$) of the sliding zone soil under different water contents were tested through laboratory tests;
2. Replace $p(\alpha_i)$ calculated by Formula (14) with Formula (25) to simplify $T_i$;
3. Jointly use (15), (16), (17), (18), and (25) to determine $\delta_0$ and $N_i$;
4. According to Formula (21), $T_{if}$ is obtained;
5. According to Formulas (22) and (23), the constitutive parameter $s_i$ is obtained, and according to Formula (8), $\delta_{peak}$ is obtained. When $\delta_i > \delta_{peak}$, $K_i = 1$; and
6. The relationship between the displacements ($\delta_{wi}$) and safety factors ($K_i$) under different moisture contents is obtained by Formula (26).

# Application of theoretical calculation methods

## An application case of model slope

### Calculation process of inclination angles of trailing edge fracture surfaces

To further illustrate the stability calculation method of progressive failure process of the two-surface retrogressive landslide, the model test slope is selected as an application example. Figure 14a is the geometric size diagram of the

landslide body. According to the working conditions, the model test is designed. The sliding zone is divided into $AB_1$, $B_1B_2$, $B_2B_3$, and $B_3B_4$. $AB_1$, $B_1B_2$, and $B_2B_3$ correspond to the sectional sliding surface range of working condition 1, working condition 2, and working condition 3 of the model test, respectively. Taking sliding mass 1 (quadrilateral $ACC_1B_1$) as an example, the bottom sliding surface is $AB_1$, and the trailing edge fracture surface is $B_1C_1$. Its stress analysis is shown in Fig. 14b, and sliding mass 2 and sliding mass 3 are shown in Fig. 14c and d, respectively.

For sliding mass 1, the length of $AB_1$ is 0.40 m, and the inclination angle $\alpha_1$ of the bottom sliding surface is 17°. When the inclination angle $\theta_1$ of the trailing edge fracture surface is known, $L_1$, $l_{W1}$, and $A_1$ can be obtained. To ensure the full search range of the inclination angle of the trailing edge fracture surface, $B_1$ is connected with C and D, and the inclination angle $\theta_1$ of the trailing edge fracture surface ranges from 33 to 113°. According to the calculation formula in the "Calculation of the new segmentation method" section, for each given $\theta_i$, there is a safety factor $F_i$, and the inclination angle of the trailing edge fracture surface corresponding to the minimum safety factor is calculated.

For sliding mass 2 and sliding mass 3, the lengths of $B_1B_2$ and $B_2B_3$ are 0.30 m, and the inclination angles of the bottom sliding surfaces are 17°. The inclination angle $\theta_2$ of the trailing edge fracture surface corresponding to $B_1B_2$ is $40 \sim 143°$, and the inclination angle $\theta_3$ of the trailing edge fracture surface corresponding to $B_2B_3$ is $56 \sim 147°$. The calculation results of the inclination angles of the trailing edge fracture surfaces are shown in Fig. 15. The safety factor $F_i$ of the sliding masses initially decreases and then increases with

**Fig. 15** Safety factors versus the inclination angles of the trailing edge fracture surfaces: **a** sliding masses 1~2; **b** sliding mass 3
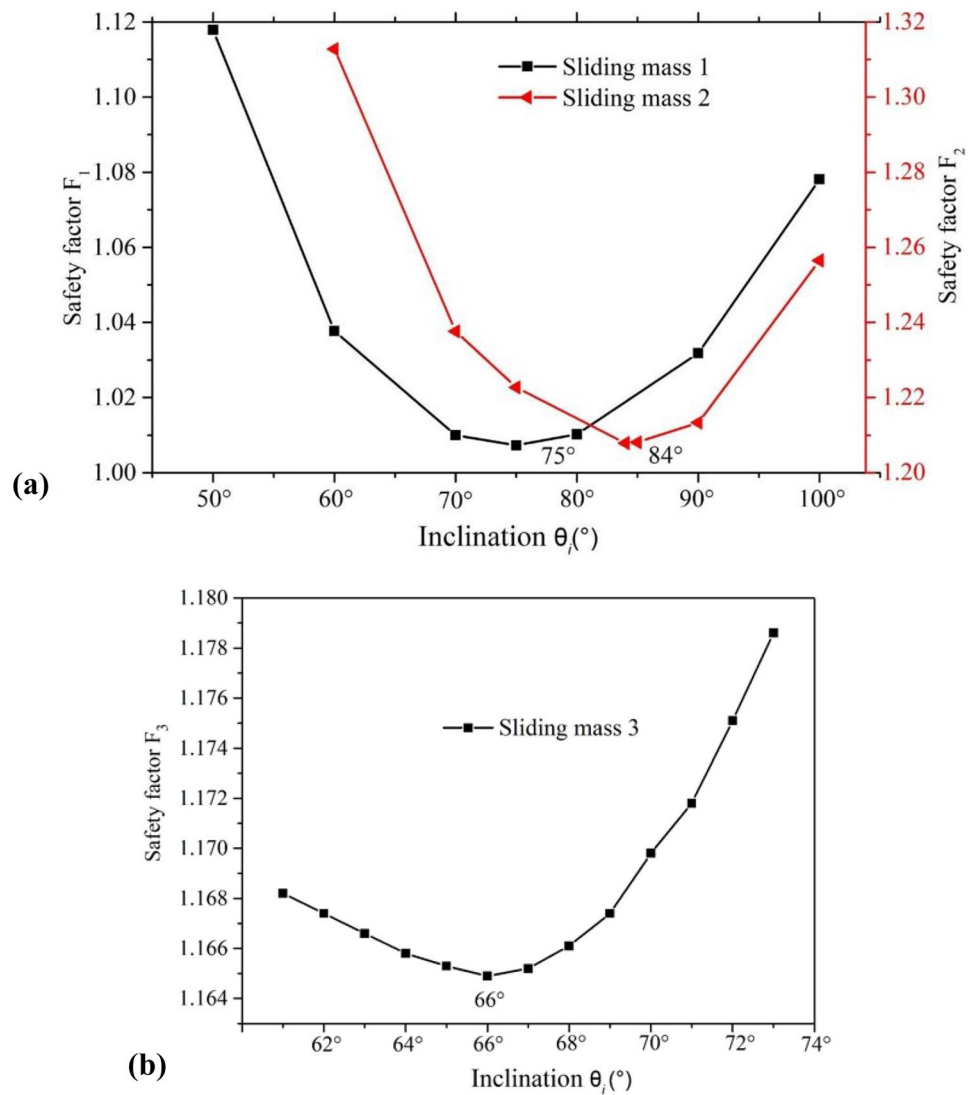


increasing $\theta_i$. Each sliding mass only has a unique minimum safety factor, which is 1.0072, 1.2079, and 1.1649, respectively. The corresponding inclination angles of the trailing edge fracture surfaces are 75°, 84°, and 66°, respectively. In Fig. 15b, only some curve values are displayed, mainly to show the lowest point values. All the calculation results of the sliding masses are shown in Table 2.

## Quantitative evaluation of horizontal displacement and safety factor

Based on obtaining the inclination angles of the trailing edge fracture surfaces of sliding masses, the stability calculation is carried out by combining the shear stress–shear displacement constitutive model of the sliding surface and the shear displacement model. In the shear stress–shear displacement constitutive model adopted in this section, $\xi$ is the parameter describing the softening characteristics, which applies to the

**Table 2** The calculated safety factor versus the inclination angle of the trailing edge fracture surface

| Sliding mass 1 | | Sliding mass 2 | | Sliding mass 3 | |
|---|---|---|---|---|---|
| $\theta_1$ | $F_1$ | $\theta_2$ | $F_2$ | $\theta_3$ | $F_3$ |
| 33° | 1.9215 | 40° | 1.9790 | 56° | 1.1812 |
| 40° | 1.3479 | 50° | 1.4905 | 60° | 1.1682 |
| 50° | 1.1179 | 60° | 1.3128 | 65° | 1.1653 |
| 60° | 1.0377 | 70° | 1.2376 | **66°** | **1.1649** |
| 70° | 1.0100 | 80° | 1.2097 | 67° | 1.1652 |
| 74° | 1.0074 | 83° | 1.2080 | 70° | 1.1786 |
| **75°** | **1.0072** | **84°** | **1.2079** | 80° | 1.2442 |
| 76° | 1.0075 | 85° | 1.2081 | 90° | 1.3728 |
| 80° | 1.0102 | 90° | 1.2133 | 100° | 1.6742 |
| 90° | 1.0318 | 100° | 1.2565 | 110° | 2.0529 |
| 100° | 1.2814 | 110° | 1.3767 | 120° | 3.0981 |
| 113° | 1.5360 | 120° | 1.4376 | 130° | 9.1418 |

**Table 3** Mechanical parameters of the sliding zone soil

| $\omega$/% | $c$/kPa | $\varphi$/° | Constitutive parameter | | |
|------------|---------|-------------|------------------------|---|---|
| | | | $G$/kPa | $m$ | $\xi$ |
| 10 | 28.24 | 19.56 | 4435 | 2 | −0.50 |
| 15 | 26.74 | 17.32 | 3265 | 2 | −0.55 |
| 20 | 21.30 | 15.03 | 2580 | 2 | −0.60 |
| 25 | 16.12 | 13.45 | 1647 | 2 | −0.65 |
| 30 | 3.68 | 9.95 | 732 | 2 | −0.70 |

sliding zone soil with strain-softening characteristics. To fully reflect the strength attenuation process of the sliding zone soil, the water content of the sliding zone soil is introduced into the calculation process to reflect the influence of water content change on the strain-softening features of sliding zone materials. The constitutive parameters of the sliding zone soil are shown in Table 3. According to the formula in the "Study on the shear stress−shear displacement constitutive model of the sliding surface" section, the $\tau$-$\delta$ characteristic curve is obtained as shown in Fig. 16. In Fig. 16, the sliding zone soil shows typical strain softening characteristics, and the shear strength decreases with increasing water content.

In Fig. 16, with the increase in the water content of the sliding zone soil, the softening coefficient decreases gradually, and the peak strength of the curve decreases continuously. In this process, the softening part of the landslide began to deform, the main crack was first produced and continuously expanded, and the sliding mass was initially

formed. With the increase in deformation, secondary cracks were produced and developed.

According to the calculation method in the "Stability analysis of two-surface progressive failure (TSPFM)" section, the relationship between the safety factors of sliding masses and the horizontal displacement curves under the different water contents can be obtained, as shown in Fig. 17 (the number on the curve represents the water content of the sliding zone soil). The safety factors of sliding masses decrease with increasing horizontal displacement. The maximum horizontal displacement of sliding mass 1 is approximately 43 mm, the horizontal displacement of sliding mass 2 and sliding mass 3 is relatively small, and the maximum displacement values are 28 mm and 24 mm, respectively. The displacement value of sliding mass 1 is the largest, the displacement value of the back sliding mass of the slope is smaller, and the stability is better. As the water content of the sliding zone soil increases gradually, the safety factor of sliding mass decreases, indicating that the strain-softening characteristics of the sliding zone soil have an important influence on the progressive failure process of the landslide.

## Comparison with test methods

### Inclination angles of the trailing edge fracture surfaces

Using the calculation method for the inclination angle of the trailing edge fracture surface in the "New method of strip partition" section, the calculated inclination angles of

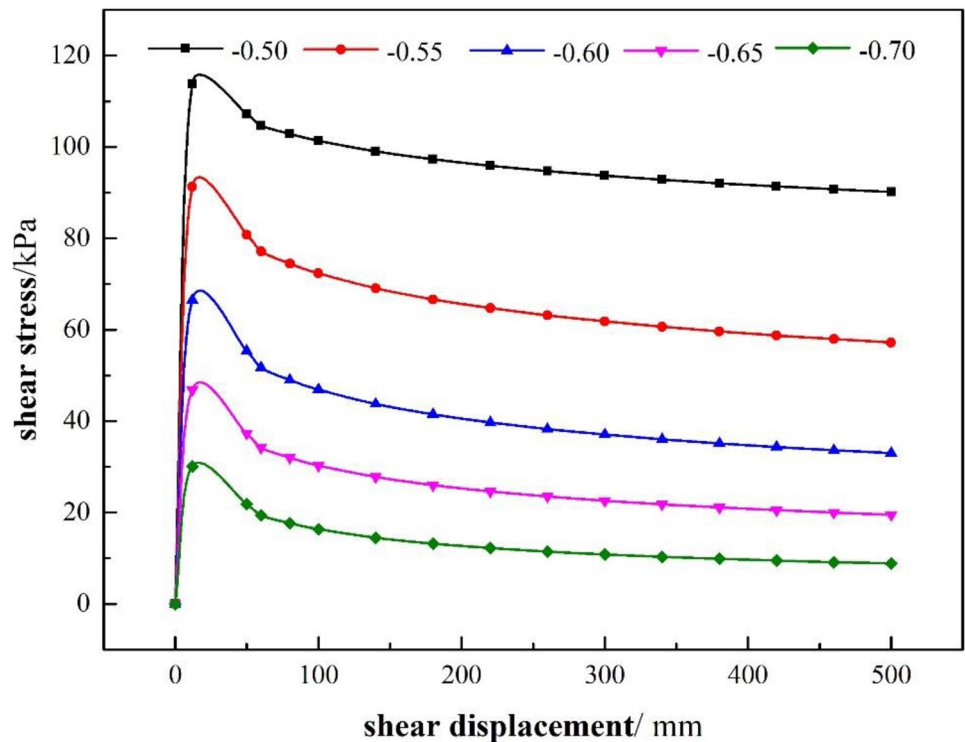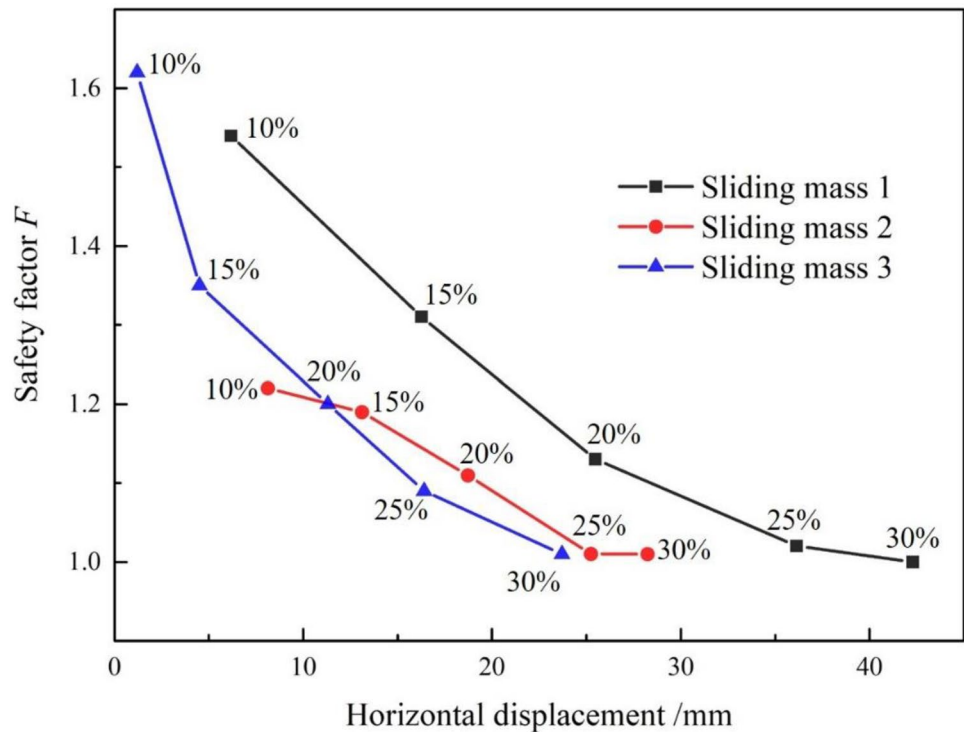**Fig. 16** Curve characteristics of the constitutive model

**Fig. 17** Relationship between the safety factors and horizontal displacements of sliding masses



sliding mass 1, sliding mass 2, and sliding mass 3 are 75°, 84°, and 66°, respectively, and the experimental values are 76°, 83°, and 72°, respectively. To verify the effectiveness of the calculation method, the relative error is used for characterization, and the relative error is defined as $R_\theta$:

$$R_\theta = \frac{\theta_t - \theta_c}{\theta_c} \qquad (27)$$

where $\theta_c$ is the calculated value of the inclination angle and $\theta_t$ is the experimental value of the inclination angle.

According to Formula (27), the relative errors between the test values and the calculated values of the SMs are 1.33%, 1.19%, and 9.09%, respectively. The relative errors of sliding mass 1 and sliding mass 2 are small, and the relative error of sliding mass 3 is large. The reason is that sliding mass 3 of the model test is close to the box, and the boundary effect is noticeable, which has a significant influence on the test value and leads to a significant error. In general, this difference is small and will not have a great impact on the actual project. The calculation method in this paper is applicable.
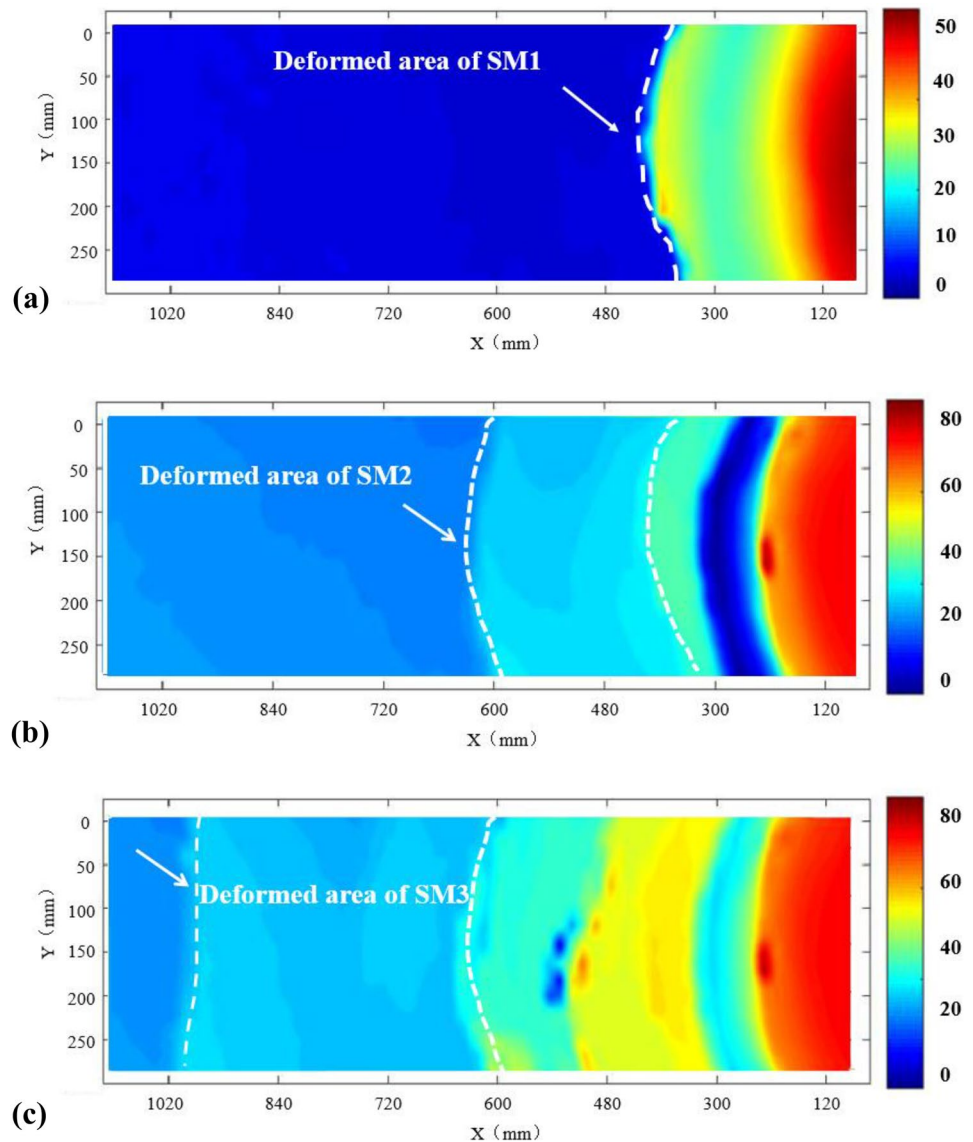
**Horizontal displacements of sliding masses**

To further verify the calculation results of horizontal displacements, this paper uses GeoPIV-RG image processing technology to process the horizontal displacement images of model test. The analysis results are shown in Fig. 18 (White et al. 2016; Li et al. 2018).

In Fig. 18a, the maximum displacement of sliding mass 1 appears near the toe of the slope, reaching 50 mm, and the horizontal displacement of the rear side of sliding mass 1 is relatively slight, which is in the range of 20~30 mm. In Fig. 18b, the horizontal displacement of sliding mass 2 is in the range of 20~40 mm. Due to the forward slip of sliding mass 2, the cumulative displacement of sliding mass 1 increases again, and the maximum value reaches 80 mm. In Fig. 18c, the horizontal displacement of sliding mass 3 is mainly concentrated in the range of 20~30 mm, and the displacement distribution is relatively uniform, indicating that the overall slip occurs at this time. With the forward sliding of sliding mass 3, the cumulative displacements of sliding mass 1 and sliding mass 2 continue to increase. At this time, the formation and development of secondary sliding masses are aggravated due to the uneven stress distribution and inconsistent deformation in the sliding masses. After all working conditions, the maximum cumulative displacement of sliding mass 1 reaches 80 mm, the maximum cumulative displacement of sliding mass 2 reaches 60 mm, and the maximum displacement of sliding mass 3 is 30 mm.

Figure 18 shows that the displacement of the model slope has prominent zoning characteristics. The cumulative displacement of sliding mass 1 is the largest, and the stability is the worst. The smaller the displacement toward the rear of the slope is, the higher the stability is. Generally, overall sliding occurs at the initial stage of the deformed slope, forming unstable sliding masses. As the deformation intensifies, it gradually decomposes into

**Fig. 18** Horizontal displacements of model slope: **a** sliding mass 1; **b** sliding mass 2; **c** sliding mass 3

multiple secondary sliding masses. The above conclusions are confirmed in previous studies (Sun et al. 2016), as shown in Fig. 19.

The theoretical results of horizontal displacement are compared with the experimental results. In the initial deformation stage, the difference in horizontal displacement is slight. Due to the multistage cumulative displacement of sliding masses 1 and 2, the experimental value of horizontal displacement is greater than the theoretical calculation value.

Due to the influence of the size effect and contact friction in the test process, there will be some errors. However, the conclusions obtained by the two methods tend to be consistent, which supports the applicability of the theoretical calculation method and preliminarily realizes the quantitative relationship between the horizontal displacement and the safety factor.

# Application of theoretical calculation method in engineering practice

## Calculation of landslide case with known bottom sliding surface

In this paper, the stability calculation of the model slope is based on the known length and inclination angle of the bottom sliding surface, and the inclination angle of the trailing edge fracture surface is calculated. In practical engineering, the length of the bottom sliding surface cannot be directly obtained. It is necessary to determine the extension range of the bottom sliding surface and the location of the surface cracks through field surveys and drilling. Figure 10 shows the retrogressive landslide caused by reservoir softening (Xu et al. 2014). The path of the bottom sliding surface depends on the interface between the weathered shale and
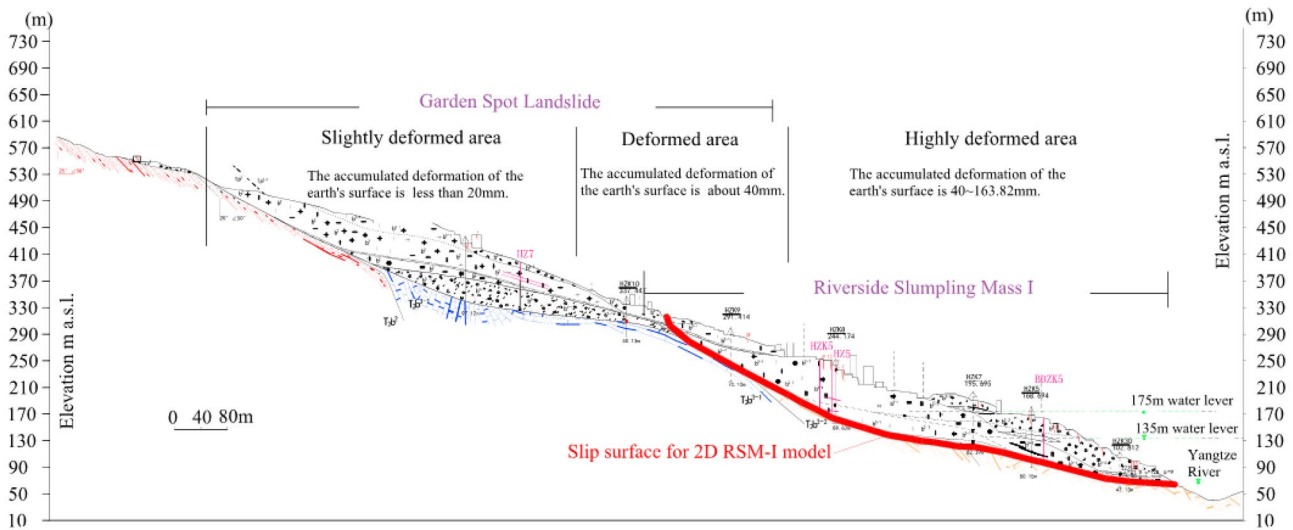
**Fig. 19** The geological profile of the Huangtupo landslide (Sun et al. 2016)

its overlying soil. Combined with the water level survey information, the morphology and sliding path of the bottom sliding surface can be preliminarily determined, and the inclination angles of the trailing edge fracture surfaces can be calculated accordingly.

Based on obtaining the inclination angles of the trailing edge fracture surfaces of the sliding masses, the mechanical parameters and constitutive parameters of the sliding zone soil are tested through field soil sampling, and the displacements of the sliding masses and the corresponding safety factors can be calculated.

## Stability calculation of landslides in engineering practice

In this section, the retrogressive landslide caused by water-induced weakening is selected for analysis, as shown in Fig. 20. The landslide is due to rainfall infiltration into the internal cracks of the slope, which leads to a decrease in the shear strength of the soil and a weakening of the saturated soil in the sliding zone. In addition, the excavation of the slope toe leads to a decrease in the sliding resistance, thus

inducing instability. The saturated weakening of the sliding zone soil is an important triggering factor.

Figure 20 shows the deformed landslide, in which the deformation of sliding mass 1 and sliding mass 2 is relatively large, and the sliding distance is rather long. The deformation of the other five sliding masses is relatively small, and the sliding distance is short. The actual sliding distance of the landslide is approximately 1.2 m (Xu et al. 2014).

To verify the practicability of the calculation method in this paper, the soil parameters of the landslide model (Xu et al. 2014) are used to calculate the inclination angles of the trailing edge fracture surfaces of seven sliding masses, as shown in Fig. 21. In Fig. 21, there is a unique minimum safety factor for every sliding mass, and the safety factor corresponds to the unique inclination angle of the trailing edge fracture surface. The safety factors $F_i$ of all curves decrease at first and then increase with increasing inclination angle $\theta_i$. The calculated value and the actual value of the inclination angles of the trailing edge fracture surfaces are shown in Table 4. The relative errors of the inclination angle of SM1 and SM2 are very large because SM1 and SM2 have undergone long-distance rotation slip. That is, the trailing edge fracture surface predicted by the original

**Fig. 20** The cross-sectional view of a real soil landslide located in Xin'an town, Pingshan County, China (Xu et al. 2014)
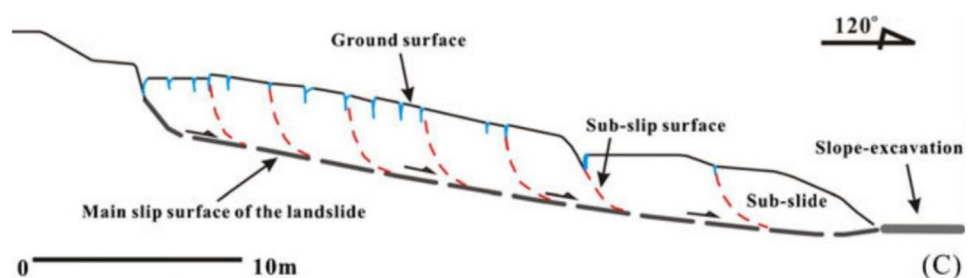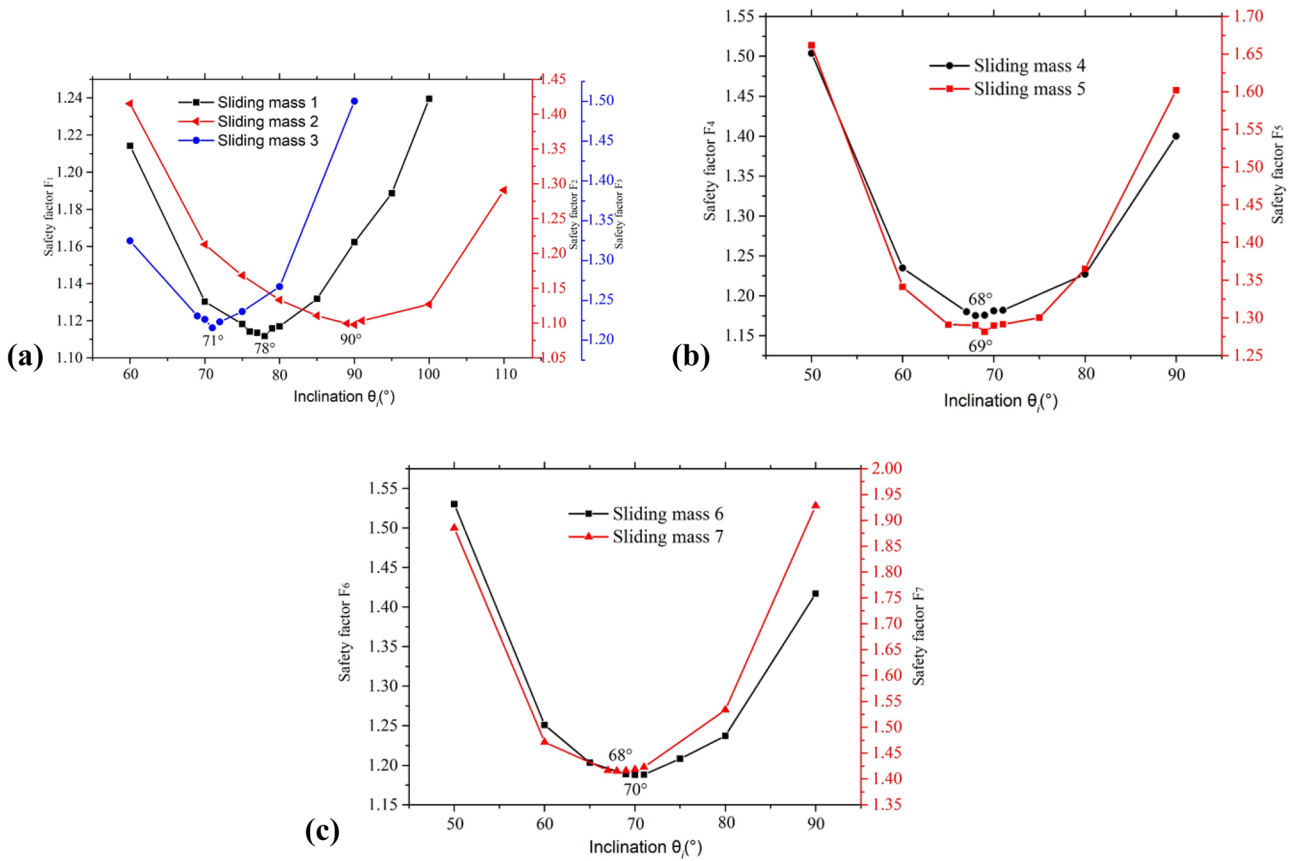
**Fig. 21** The calculated safety factors versus the inclination angles of the trailing edge fracture surfaces in the seven sliding masses: **(a)** sliding masses 1~3; **(b)** sliding masses 4~5; **(c)** sliding masses 6~7

slope has experienced a long-distance rotation slip and developed into the present form. Due to the small deformation of SM3~SM7, the relative errors of the inclination angles are small, ranging from 1.45 to 10.94%. The results show that the calculation method of the inclination angles of the trailing edge fracture surfaces proposed in this paper is more suitable for the slope in the limit equilibrium state or small deformation stage and is not suitable for the slope with large deformation.

The calculated horizontal displacements of all sliding masses are shown in Table 4. The sum of the displacements is 117.2 mm, which is slightly different from the actual measured value of 120 mm. According to the calculated value of the horizontal displacement and the inclination angle of the trailing edge fracture surface of each sliding mass, it is speculated that the slope shape before deformation is shown in Fig. 22. In Fig. 22, the blue boundary line is the slope model before deformation, and the red boundary line is

**Table 4** The calculated inclination angles and displacement

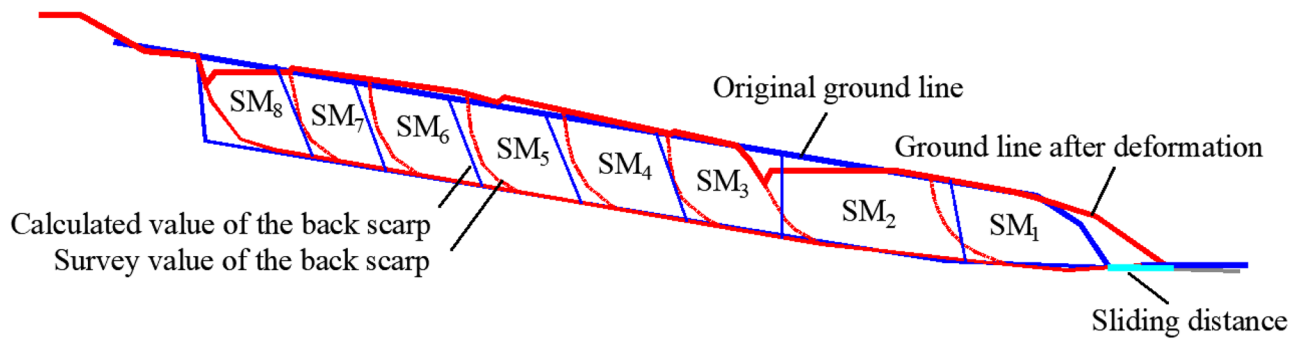| Number of sliding mass | Calculated inclination angle/° | Original reference/° | Relative error/% | Calculated displacement/ mm | Calculated total displacement | Original reference total displacement |
|---|---|---|---|---|---|---|
| 1 | 78 | 56 | 39.28 | 26.6 | | |
| 2 | 90 | 54 | 66.67 | 33.7 | | |
| 3 | 71 | 64 | 10.94 | 16.2 | 117.2 mm | 120.0 mm |
| 4 | 68 | 63 | 7.94 | 13.9 | | |
| 5 | 69 | 67 | 2.99 | 12.7 | | |
| 6 | 68 | 65 | 4.62 | 8.4 | | |
| 7 | 70 | 69 | 1.45 | 5.7 | | |

**Fig. 22** The cross-sectional view of pre-deformation slope versus deformed slope

the slope model after deformation. In general, the inclination errors of the trailing edge fracture surfaces of sliding masses with large deformation are more significant (SM1 ~ SM2), and the inclination errors of the sliding masses with small deformation are more minor (SM3 ~ SM7). The final total displacement error is small, indicating that the TSPFM method in this paper is applicable. Of course, more landslide examples are needed to verify the accuracy and feasibility of this method.

## Discussion on the application of the TSPFM method

The application of the TSPFM method is first to calculate the possible inclination angle of the trailing edge fracture surface of landslide instability according to the existing survey data. However, the survey data of many landslides are unknown, and the geometric shape and length of the bottom sliding surface cannot be directly obtained. At this time, the position of the trailing edge scarps observed on the surface can be used as a known parameter, and the inclination angle range of the trailing edge fracture surface can be calculated by assuming the geometric function of the bottom sliding surface to obtain the information of the bottom sliding surface. This method is helpful for targeted bottom geological exploration operations, such as deformation monitoring and exploration coring. More importantly, the inclination angle of the trailing edge fracture surface can guide the strip division of the actual landslide and improve the accuracy of landslide stability analysis, which is of great significance for landslide thrust calculation and targeted support.

In addition, the TSPFM method can characterize the correlation between horizontal displacement and landslide stability and evaluate the stability of landslides based on macroscopic deformation. In the process of field investigation, the deformation information of landslides can be obtained directly, and the trend of stability can be speculated and predicted.

It is verified by the landslide example that the TSPFM method is more suitable for the calculation of the inclination

angle of the trailing edge fracture surface for retrogressive landslides in the limit equilibrium state or with small deformation, and it is not suitable for the sliding mass that has undergone rotation slip or large deformation. In addition, there are many forms of bottom sliding surfaces in nature. If the bottom sliding surface is not an approximate plane but a curved surface or irregular shape, a derivative calculation method can be introduced to calculate the bottom sliding surface. However, the mathematical calculation of this method is difficult and needs further discussion.

## Conclusion

Quantitative evaluation of landslide stability is a very important part of geological disaster assessment. In this paper, the failure mechanism and stability characteristics of water-induced weakening retrogressive landslides are discussed in depth by combining model tests with theoretical analysis. The main research results are as follows.

The designed and developed model test device of the "segmented sliding surface bottom permeation method" reproduces the retrogressive landslide induced by water-induced weakening and the multistage sliding masses formed in this process well. The test results show that the water-induced weakening retrogressive landslide presents a typical two-surface progressive failure mechanism. That is, due to the soil saturation weakening in the bottom sliding zone, the shear strength decreases, and the bottom sliding surface is gradually formed. Subsequently, the deformed slope on the sliding surface slides to form the trailing edge fracture surface.

The inclination angles of trailing edge fracture surfaces are all steep dip angles of 66 ~ 90°. The relative error between the theoretical and experimental values of the inclination angles of the trailing edge fracture surfaces of 3 sliding masses for the model test is 1.33 ~ 9.09%, the relative error between the theoretical and measured values of the small deformation sliding masses (SM3 ~ SM7) of the

actual landslide is 1.45 ~ 10.94%, and the error of the sliding masses (SM1 and SM2) with large rotation slip is large. The TSPFM method is suitable for calculating the inclination angles of the trailing edge fracture surfaces under the limit equilibrium state or small deformation and has high accuracy.

The instability range of the sliding zone directly affects the deformation area of the landslide. The horizontal displacement of sliding masses at all levels has obvious zoning characteristics, and there are secondary sliding masses. The TSPFM method can perform the quantitative evaluation between the horizontal displacement and the safety factor. With the increase in the moisture content of the sliding zone soil, the larger the horizontal displacement of the sliding mass is, the smaller the safety factor. The actual landslide is selected for calculation, and the relative error between the calculated value of the total horizontal displacement and the measured value is 2.33%, which verifies the applicability of the theoretical method.

The test method in this paper should be further developed and improved, considering a variety of soil conditions, landslide types, sliding zone morphology and slope morphology, and other factors. At present, the theoretical calculation method only selects the approximate plane slip band for calculation, and the shape of the surface or irregular slip band is less considered. The theoretical analysis of this part needs to be further strengthened, which will be shown in subsequent research.

## Declarations

**Competing interest**  The authors declare no competing interests.

## References

Alimohammadlou Y, Najafi A, Gokceoglu C (2014) Estimation of rainfall-induced landslides using ANN and fuzzy clustering methods: a case study in Saeen Slope, Azerbaijan province. Iran Catena 120:149–162. https://doi.org/10.1016/j.catena.2014.04.009

Amini M, Ardestani A, Khosravi MH (2017) Stability analysis of slide-toe-toppling failure. Eng Geol 228:82–96. https://doi.org/10.1016/j.enggeo.2017.07.008

Azarafza M, Akgün H, Atkinson PM, Derakhshani R (2021a) Deep learning-based landslide susceptibility mapping. Sci Rep 11(1):1–16. https://doi.org/10.1038/s41598-021-03585-1

Azarafza M, Akgün H, Ghazifard A, Asghari-Kaljahi E, Rahnamarad J, Derakhshani R (2021b) Discontinuous rock slope stability analysis by limit equilibrium approaches-a review. Int J Digi Earth 14(12):918–1941. https://doi.org/10.1080/17538947.2021.1988163

Azarafza M, Asghari-Kaljahi E, Akgün H (2017) Assessment of discontinuous rock slope stability with block theory and numerical modeling: a case study for the South Pars Gas Complex, Assalouyeh. Iran Environ Earth Sci 76(11):397. https://doi.org/10.1007/s12665-017-6711-9

Azarafza M, Zhu HH (2022) Key-block theorem application on discontinuous rock slope instabilities and rock mass description. In Belt and road webinar series on geotechnics, energy and environment. 200–208. https://doi.org/10.1007/978-981-16-9963-4

Ding Y, Dang C, Yuan GX, Wang QC (2012) Characteristics and remediation of a landslide complex triggered by the 2008 Wenchuan, China earthquake-case from Yingxiu near the earthquake epicenter. Environ Earth Sci 67:161–173. https://doi.org/10.1007/s12665-011-1489-7

Graber A, Santi P, Arestegui PM (2021) Constraining the critical groundwater conditions for initiation of large, irrigation-induced landslides, Siguas River Valley. Peru Landslides 18(12):3753–3767. https://doi.org/10.1007/s10346-021-01767-6

Guo C, Zhang Y, Li X, Ren S, Yang Z, Wu R, Jin J (2020a) Reactivation of giant Jiangdingya ancient landslide in Zhouqu County, Gansu Province, China. Landslides 17:179–190. https://doi.org/10.1007/s10346-019-01266-9

Guo J, Xu M, Zhang Q, Xiao XX, Zhang SS, He SM (2020b) Reservoir regulation for control of an ancient landslide reactivated by water level fluctuations in Heishui River. China J Earth Sci 31(6):1058–1067. https://doi.org/10.1007/s12583-020-1341-7

He C, Hu X, Tannant DD, Tan F, Zhang Y, Zhang H (2018) Response of a landslide to reservoir impoundment in model tests. Eng Geol 247:84–93. https://doi.org/10.1016/j.enggeo.2018.10.021

Huang CC (2013) Developing a new slice method for slope displacement analyses. Eng Geol 157:39–47. https://doi.org/10.1016/j.enggeo.2013.01.018

Huang D, Gu DM, Song YX, Cen DF, Zeng B (2018) Towards a complete understanding of the triggering mechanism of a large reactivated landslide in the Three Gorges Reservoir. Eng Geol 238:36–51. https://doi.org/10.1016/j.enggeo.2018.03.008

Huang D, Luo SL, Zhong Z, Gu DM, Song YX, Tomás R (2020) Analysis and modeling of the combined effects of hydrological factors on a reservoir bank slope in the Three Gorges Reservoir area, China. Eng Geol 279:105858. https://doi.org/10.1016/j.enggeo.2020.105858

Hu XL, Zhang M, Sun MJ, Huang KX, Song YJ (2015) Deformation characteristics and failure mode of the Zhujiadian landslide in the Three Gorges Reservoir, China. Bull Eng Geol Environ 74:1–12. https://doi.org/10.1007/s10064-013-0552-x

Jiang Q, Cui J, Feng XT, Jiang YJ (2014) Application of computerized tomographic scanning to the study of water-induced weakening of mudstone. Bull Eng Geol Env 73(4):1293–1301. https://doi.org/10.1007/s10064-014-0597-5

Kainthola A, Verma D, Thareja R, Singh TN (2013) A review on numerical slope stability analysis. Int J Sci Eng Technol Res (IJSETR) 2(6):1315–1320

Kennedy R, Take WA, Siemens G (2021) Geotechnical centrifuge modeling of retrogressive sensitive clay landslides. Can Geotech J 58:1452–1465. https://doi.org/10.1139/cgj-2019-0677

Kumar N, Verma AK, Sardana S, Sarkar K, Singh TN (2018) Comparative analysis of limit equilibrium and numerical methods for prediction of a landslide. Bull Eng Geol Environ 77(2):595–608. https://doi.org/10.1007/s10064-018-1247-0

Lian BQ, Peng JB, Zhan HB, Huang QB, Wang XG, Hu S (2020) Formation mechanism analysis of irrigation-induced retrogressive loess landslides. CATENA 195:104441. https://doi.org/10.1016/j.catena.2019.104441

Liao K, Wu Y, Miao F, Li L, Xue Y (2021) Effect of weakening of sliding zone soils in hydro-fluctuation belt on long-term reliability of reservoir landslides. Bull Eng Geol Env 80:3801–3815. https://doi.org/10.1007/s10064-021-02167-9

Li Q, Wang YM, Zhang KB, Yu H, Tao ZY (2020) Field investigation and numerical study of a siltstone slope instability induced by

excavation and rainfall. Landslides 17(6):1485–1499. https://doi.org/10.1007/s10346-020-01396-5

Li SJ, Sun QC, Zhang ZH, Luo XQ (2018) Physical modeling and numerical analysis of slope instability subjected to reservoir impoundment of the Three Gorges. Environ Earth Sci 77:138. https://doi.org/10.1007/s12665-018-7321-x

Liu D, Hu X, Zhou C, Xu C, He C, Zhang H, Wang Q (2020) Deformation mechanisms and evolution of a pile-reinforced landslide under long-term reservoir operation. Eng Geol. https://doi.org/10.1016/j.enggeo.2020.105747

Liu B, Wang CK, Liu ZY, Xu ZH, Nie LC, Pang YH, Wang N, Feng SX (2021) Cascade surface and borehole geophysical investigation for water leakage: a case study of the Dehou reservoir, China. Eng Geol 294:1–12. https://doi.org/10.1016/j.enggeo.2021.106364

Liu F, Li J (2015) Landslide erosion associated with the Wenchuan earthquake in the Minjiang River watershed: implication for landscape evolution of the Longmen Shan, eastern Tibetan Plateau. Nat Hazards 76(3):1911–1926. https://doi.org/10.1007/s11069-014-1575-8

Xu X, Guo WZ, Liu Y, Ma J, Wang W, Zhang H, Gao H (2017b) Landslides on the Loess Plateau of China: a latest statistics together with a close look. Nat Hazards 86:1393–1403. https://doi.org/10.1007/s11069-016-2738-6

Yin YP, Huang BL, Zhang Q, Yan GQ, Dai ZW (2020) Research on recently occurred reservoir-induced Kamenziwan rockslide in Three Gorges Reservoir, China. Landslides 17 (8):1935–1949. https://doi.org/10.1007/s10346-020-01394-7

Zou Z, Lei D, Jiang G, Luo B, Chang S, Hou C (2020) Experimental study of bridge foundation reinforced with front and back rows of anti-slide piles on gravel soil slope under El Centro Waves. Appl Sci 10:3108. https://doi.org/10.3390/app10093108

Lu Y, Huang X, Liu D (2015) Force-desplacement method of slice block analysis of slope stability and its application. Rock Soil Mecha 36 (10):2780–2786. (in Chinese)

Lu Y (2015) Deformation and failure mechanism of slope in three dimensions. J Rock Mech Geotech Eng 7(2):109–119. (in Chinese)

Lv H, Ling C, Hu B, Ran J, Zheng Y, Xu Q, Tong J (2019) Characterizing groundwater flow in a translational rock slide of southwestern China. Bull Eng Geol Environ 78(3):1989–2007. https://doi.org/10.1007/s10064-017-1212-3

Nanehkaran YA, Mao Y, Azarafza M, Kockar M K, Zhu HH (2021) Fuzzy-based multiple decision method for landslide susceptibility and hazard assessment: a case study of Tabriz, Iran. Geomech Eng 24(5):407–418. https://doi.org/10.12989/gae.2021.24.5.407

Oezdemir A, Delikanli M (2009) A geotechnical investigation of the retrogressive Yaka Landslide and the debris flow threatening the town of Yaka (Isparta, SW Turkey). Nat Hazards 49(1):113–136. https://doi.org/10.1007/s11069-008-9282-y

Pan YH, Chen JP, Wu LQ, Wang W, Tan FL (2017) Evolution mechanism and rainfall warning criteria for Maijianwo Slope in Henan Province. China Geotech Geol Eng 35(1):183–194. https://doi.org/10.1007/s10706-016-0096-5

Qi X, Xu Q, Liu F (2018) Analysis of retrogressive loess flowslides in Heifangtai. China Eng Geol 236:119–128. https://doi.org/10.1016/j.enggeo.2017.08.028

Regmi RK, Jung K, Nakagawa H, Kang J (2014) Study on mechanism of retrogressive slope failure using artificial rainfall. CATENA 122:27–41. https://doi.org/10.1016/j.catena.2014.06.001

Sarma SK (1973) Stability analysis of embankments and slopes. Geotechnique 23(3):423–433

Shan Z, Zhang W, Wang D, Wang L (2021) Numerical investigations of retrogressive failure in sensitive clays: revisiting 1994

Sainte-Monique slide, Quebec. Landslides 18:1327–1336. https://doi.org/10.1007/ss10346-020-01567-4

Spencer E (1967) A method of analysis of the stability of embankments assuming parallel inter-slice forces. Geotechnique 17(1):11–26

Sun GH, Zheng H, Tang HM, Dai FC (2016) Huangtupo landslide stability under water level fluctuations of the Three Gorges reservoir. Landslides 13(5):1167–1179. https://doi.org/10.1007/s10346-015-0637-7

Sun L, Kai C, Yixuan W (2021) Model test study on retrogressive and sliding mechanism of reservoir-reactivated landslide. Journal of Harbin Institute of Technology 53(11):162–170. (in Chinese)

Sun L, Yang T, Cheng Q, Wu D (2018) Experimental study on couse of progressive formation of retrogressive landslide. J Southwest Jiaotong Univ 53(4):762–771 (in Chinese)

Take WA, Beddoe RA, Davoodi-Bilesavar R, Phillips R (2015) Effect of antecedent groundwater conditions on the triggering of static liquefaction landslides. Landslides 12(3):469–479. https://doi.org/10.1007/s10346-014-0496-7

Thiebes B, Bell R, Glade T, Jäger S, Mayer J, Anderson M, Holcombe L (2014) Integration of a limit-equilibrium model into a landslide early warning system. Landslides 11(5):859–875. https://doi.org/10.1007/s10346-013-0416-2

Wang L, Sun DA, Li L (2019) Three-dimensional stability of compound slope using limit analysis method. Can Geotech J 56(1):116–125. https://doi.org/10.1139/cgj-2017-0345

Wang Q, Wang Z, Su Y, Zhong X, Wang L, Ma H, Zhang G, Woolery EE, Liu K (2021) Characteristics and mechanism of the landslide in Yongguang village, Minxian County, China. Nat Hazards 105:1413–1438. https://doi.org/10.1007/s11069-020-04360-7

Wang Z, Ye XM, Liu YX (2018) Improved Janbu slices method considering progressive destruction in a landslide. Rock Soil Mech 39(2):675–682 (in Chinese)

White DJ, Take W, BOLTON M A, (2016) Improved image-based deformation measurement for geotechnical application. Can Geotech J 53(5):727–739. https://doi.org/10.1139/cgj-2015-0253

Wu LZ, Huang RQ, Xu Q, Zhang LM, Li HL (2015) Analysis of physical testing of rainfall-induced soil slope failures. Environ Earth Sci 73:8519–8531. https://doi.org/10.1007/s12665-014-4009-8

Wu SC, Han LQ, Cheng ZQ, Zhang XQ, Cheng HY (2019) Study on the limit equilibrium slice method considering characteristics of inter-slice normal forces distribution: the improved Spencer method. Environ Earth Sci 78:611. https://doi.org/10.1007/s12665-019-8621-5

Xu L, Dai FC, Chen J, Iqbal J, Qu YX (2014) Analysis of a progressive slope failure in the Xiangjiaba reservoir area. Southwest China Landslides 11(1):55–66. https://doi.org/10.1007/s10346-012-0373-1

Xu Q, Liu HX, Ran JX, Li WH, Sun X (2017a) Field monitoring of groundwater responses to heavy rainfalls and the early warning of the Kualiangzi landslide in Sichuan Basin, southwestern China. Landslides 13(6):1555–1570. https://doi.org/10.1007/s10346-016-0717-3

Zhang S, Xu Q, Hu ZM (2016) Effects of rainwater softening on red mudstone of deep-seated landslide, Southwest China. Eng Geol 204:1–13. https://doi.org/10.1016/j.enggeo.2016.01.013